

Dark matter at DeepCore and IceCube

V. Barger¹, Y. Gao², D. Marfatia^{3,1}

¹*Department of Physics, University of Wisconsin, Madison, WI 53706, U.S.A.*

²*Department of Physics, University of Oregon, Eugene, OR 97403, U.S.A.*

³*Department of Physics and Astronomy, University of Kansas, Lawrence, KS 66045, U.S.A.*

Abstract

With the augmentation of IceCube by DeepCore, the prospect for detecting dark matter annihilation in the Sun is much improved. To complement this experimental development, we provide a thorough template analysis of the particle physics issues that are necessary to precisely interpret the data. Our study is about nitty-gritty and is intended as a framework for detailed work on a variety of dark matter candidates. To accurately predict the source neutrino spectrum, we account for spin correlations of the final state particles and the helicity-dependence of their decays, and absorption effects at production. We fully treat the propagation of neutrinos through the Sun, including neutrino oscillations, energy losses and tau regeneration. We simulate the survival probability of muons produced in the Earth by using the Muon Monte Carlo program, reproduce the published IceCube effective area, and update the parameters in the differential equation that approximates muon energy losses. To evaluate the zenith-angle dependent atmospheric background event rate, we track the Sun and determine the time it spends at each zenith angle. Throughout, we employ neutralino dark matter as our example.

I. INTRODUCTION

Astrophysical data require about 20% of the energy density of our universe to be in the form of unseen matter. The nature of this *dark matter* (DM) is a mystery that is key to resolving several problems in astrophysics and cosmology. A possibility is that DM consists of stable or very long-lived Weakly Interacting Massive Particles (WIMPs). However, there is no such particle in the spectrum of the Standard Model (SM) of particle physics and a wide range of new physics models have been proposed to introduce WIMP candidates. The most popular scenarios include supersymmetry (SUSY), extra dimensions, and n -plet extended models ($n \geq 1$).

SUSY with \mathcal{R} -parity [1] is a well motivated possibility that alleviates the hierarchy problem, realizes gauge coupling unification and facilitates the seesaw mechanism of neutrino mass generation when augmented with right-handed neutrinos. \mathcal{R} -parity conserving SUSY provides the lightest \mathcal{R} -odd particle as a WIMP candidate. The cosmic microwave background data from Wilkinson Microwave Anisotropy Probe (WMAP) [2] pins down the relic dark matter abundance to be $\Omega_{DM}h^2 = 0.1123 \pm 0.0035$, which stringently constrains the SUSY parameter space. The popular minimal supergravity model [3] (mSUGRA) is defined by a set of only five parameters.

Indirect searches look for cosmic ray excesses in the diffuse background or from point sources due to DM annihilation or decay into SM particles. Due to their high penetration ability, neutrinos help with detecting DM deep inside gravitational wells that include nearby sources like the Sun, the Earth and the galactic center [4–6]. DM-induced neutrinos from the Sun can be observed if the signal rate is competitive with the atmospheric neutrino flux, which is created by collisions of cosmic protons and nuclei in the atmosphere and is the dominant background below a TeV.

Among the many experiments searching for high energy neutrinos, we focus on the IceCube (IC) detector [7] that is capable of observing neutrinos with energies above 100 GeV. The installment of DeepCore [8] (DC) significantly lowers IceCube’s energy threshold and enhances the ability of detecting neutrinos from light WIMP annihilation. We carry out a detailed simulation of IC/DC detection of the neutrino signal from neutralino annihilation in the Sun for the sample relic-density-consistent mSUGRA points listed in Table I in standard

Point	m_0	$m_{1/2}$	A_0	$\tan\beta$	m_{χ^0}	$\tau^+\tau^-$	W^+W^-	ZZ	$b\bar{b}$	$c\bar{c}$	$t\bar{t}$	Ann./yr
A (Focus Point)	2154	288	0	10	105	—	90%	8.4%	1.0%	0.11%	—	5.4×10^{22}
B	2268	488	0	50	197	1.3%	12%	5.4%	9.5%	—	69%	4.4×10^{21}
C ($\tilde{\tau}$ co-ann.)	54	241	0	10	93	16%	4.4%	—	76%	—	—	2.3×10^{21}
D (A -funnel)	483	304	0	50	123	12%	—	—	88%	—	—	2.7×10^{21}
E (\tilde{t} co-ann.)	150	302	-1099	5	121	95%	0.24%	—	2.9%	—	—	1.2×10^{18}
F (Bulk)	80	170	-250	10	64	36%	—	—	63%	—	—	7.7×10^{21}
G (h -funnel)	2000	130	-2000	10	55	7.4%	—	—	83%	3.5%	—	4.4×10^{16}

TABLE I. Sample points in regions of mSUGRA parameter space that are compatible with the dark matter relic abundance; the sign of the μ parameter is positive and the top quark mass is 172.7 GeV. The lightest neutralino χ^0 is the WIMP candidate. Points A–D are selected to have $m_{\chi^0} \sim 10^2$ GeV and large annihilation rates from parameter scans with $\tan\beta = 10$ and 50. Points E–G are representative relic density compatible points from Ref. [9]. Masses are in GeV, and the last column gives the number of annihilations per year in the Sun. Only channels with branching fractions larger than 10^{-3} are listed.

notation; for a review of the various parameter regions see Ref. [10].

In Section II we summarize the physics of DM condensation and annihilation in the Sun. In Section III we describe our calculation of the spin correlated neutrino source spectrum and its propagation from the Solar core to the Earth. In Section IV we discuss the simulation of neutrino-induced events at the IC/DC detector. We present our results in Section V and summarize in Section VI. In 5 appendices, we provide several details of our calculations.

II. DM CAPTURE AND ANNIHILATION

As the Sun sweeps through the dark matter halo, WIMPs collide with solar nuclei and become gravitationally trapped. The capture over a long period of time leads to condensation of low-speed WIMPs in the center of the Sun. The capture rate [5] C_C receives contributions from spin-independent (SI) and spin-dependent (SD) scattering between WIMPs and nuclei. Then, $C_C = C_C^{SI} + C_C^{SD}$ with [11]

$$C_C^{SI} = 4.8 \times 10^{28} s^{-1} \frac{\rho_{0.3}}{\bar{v}_{270} m_{\chi^0}} \sum_i F_i f_i \phi_i \frac{\sigma_i^{SI}}{m_{N_i}} S \left(\frac{m_{\chi^0}}{m_{N_i}} \right), \quad (1)$$

$$C_C^{SD} = 1.3 \times 10^{29} s^{-1} \frac{\rho_{0.3}}{\bar{v}_{270} m_{\chi^0}} \sigma_H^{SD} S \left(\frac{m_{\chi^0}}{m_{N_i}} \right), \quad (2)$$

where i sums over the elements with significant abundance in the Sun ranging from hydrogen to iron. $\rho_{0.3}$ is the local DM halo density in units of 0.3 GeV/cm^3 , \bar{v}_{270} is the average DM dispersion velocity in units of 270 km/s , m_{N_i} denotes the mass of the nucleus of the i^{th} element in GeV , and σ_i is the SD/SI scattering cross section in pb. f_i, F_i and S are the mass fraction, kinematic suppression and form-factor suppression [12] for nucleus i , respectively. ϕ_i describes the distributions of the i^{th} element. We refer interested readers to Ref. [11] for a detailed discussion and the values for these parameters. For most mSUGRA points consistent with the measured relic density, σ^{SD} is greater than σ^{SI} by two to three orders of magnitude, but does not necessarily dominate the capture rate.

As the density builds up in the center of the Sun the annihilation of DM particles occurs more frequently. Eventually equilibrium sets in, $C_C = 2C_A$, where C_A is the annihilation rate. However, it was pointed out in Ref. [13] that large areas of SUSY parameter space do not saturate this equilibrium condition and C_A can be significantly below $C_C/2$. The DM annihilation rate in the Sun [14] and can be parametrized by [11]

$$C_A = \frac{C_C}{2} \tan^2(t/\tau), \quad (3)$$

$$t/\tau = 330 \left[\frac{C_C}{s^{-1}} \frac{\langle \sigma_A v \rangle}{\text{cm}^3 \text{s}^{-1}} \left(\frac{m_{\chi^0}}{10 \text{ GeV}} \right)^{0.75} \right]^{\frac{1}{2}},$$

where t and τ denote the age of the Sun and the equilibrium time scale, and $\langle \sigma_A v \rangle$ is the annihilation cross section averaged over the velocity distribution in the nonrelativistic limit. We do not assume that equilibrium holds, and calculate the annihilation rate for each region.

III. NEUTRINO SOURCE SPECTRA AND PROPAGATION

The source neutrino/antineutrino flux is

$$\frac{d\phi_\nu}{dE_\nu} = C_A \sum_i \text{BF}_i \frac{d\phi_\nu^i}{dE_\nu}, \quad (4)$$

where i denotes each annihilation channel, and BF_i and $\frac{d\phi_\nu^i}{dE}$ are the corresponding branching fractions and normalized (to each annihilation event) neutrino energy spectra, respectively.

The dominant annihilation channels for our sample mSUGRA points are provided in Table I. Note that the evolution of the mSUGRA renormalization group equations (RGEs) to the weak scale can be numerically sensitive to the GUT-scale parameters and lead to significant uncertainty in the annihilation rate. This is especially true for the Focus Point region. We use DarkSusy [15] to calculate $\langle\sigma_A v\rangle$ and $\sigma_{p,n}^{SI,SD}$, needed to determine the annihilation rate.

Since neutralinos are Majorana fermions, their annihilation into light fermion pairs is helicity-suppressed in the nonrelativistic limit. Thus WIMP-induced neutrinos do not have a line spectrum in mSUGRA. The dominant neutrino source is the annihilation into gauge bosons, 2^{nd} and 3^{rd} generation fermions, and their subsequent decays. Spin-correlation effects are visible in the neutrino energy spectrum, especially in the case of gauge bosons for which final states with transverse polarizations dominate in the static limit. It is important to carry out a spin-correlated calculation since the transversely polarized WW channel produces a significantly harder neutrino spectrum than the longitudinal WW channel. Similarly, a left-handed τ produces more neutrinos than a right-handed τ . In our analysis, we retain the spins of particles that directly result from the decay of particles pair-produced in DM annihilation. Secondary neutrinos arise from subsequent decays, and we include the spin correlation in helicity-dependent τ decays. At this level the spin information of the primary and major secondary neutrino contributions are taken into account. The s -channel top-pair final state can be significant for large neutralino masses, and the polarization of the on-shell W from top decay affects the leading neutrino distribution. For this particular channel we proceed to the next level and keep the spins of the decay products of the W . See Appendices A and B for a discussion of our simulation of the various annihilation channels.

The dense solar matter absorbs all the muons and relatively long-lived hadrons. A large fraction of c, b hadrons also scatter before they can decay. Thus muons are considered the end of the cascade and do not contribute to the neutrino flux. The absorption probability of c, b hadrons is determined by the competition between scattering and decay rates, which is discussed in Appendix C.

The low flux density at the center of the Sun means neutrinos are created incoherently in

the flavor basis. Following Ref. [16], we treat the neutrino propagation through the Sun with the flavor-density matrix $\boldsymbol{\rho}_{ij}$ that denotes the distribution in the flavor basis ($i, j = \nu_e, \nu_\mu, \nu_\tau$). The propagation is governed by the equation,

$$\frac{d\boldsymbol{\rho}}{dr} = -i [\mathbf{H}, \boldsymbol{\rho}] - \left. \frac{d\boldsymbol{\rho}}{dr} \right|_{NC, CC}, \quad (5)$$

where r is the distance from the center of the Sun. The $\frac{d\boldsymbol{\rho}}{dr}$ term denotes the neutrino flux attenuation from neutral-current (NC) and charged-current (CC) scatterings off the solar matter, and ‘re-injection’ at lower energy after NC scattering, as well as secondary ν_e, ν_μ production from τ regeneration; see Appendix D for details. As neutrinos are created in gauge eigenstates, $\boldsymbol{\rho}$ is a diagonal matrix at the center of the Sun with diagonal elements ρ_{ii} denoting the fractions of the corresponding flavor. The flavor-basis Hamiltonian includes a rotation from a diagonal mass basis matrix and a matter effect term due to CC scattering with electrons [17],

$$\mathbf{H} = \frac{1}{2E_\nu} \mathbf{V} \mathbf{diag} (0, \delta m_{21}^2, \delta m_{31}^2) \mathbf{V}^\dagger \pm \sqrt{2} G_F n_e \mathbf{diag} (1, 0, 0), \quad (6)$$

where n_e is the electron number density, G_F is the Fermi constant, and $\delta m_{ij}^2 = m_i^2 - m_j^2$ are the neutrino mass-squared differences. The sign of the matter term is positive for neutrinos and negative for antineutrinos. \mathbf{V} is the neutrino mixing matrix parametrized by three mixing angles θ_{ij} and a CP phase. We set the oscillation parameters to be [18]:

$$\delta m_{21}^2 = 8.1 \times 10^{-5} \text{ eV}^2, \quad \delta m_{31}^2 = 2.2 \times 10^{-3} \text{ eV}^2, \quad \theta_{12} = 33.2^\circ, \quad \theta_{13} = 0, \quad \theta_{23} = 45^\circ. \quad (7)$$

After leaving the surface of the Sun, neutrino propagation is dictated by the vacuum Hamiltonian $H|_{n_e=0}$. Our choice $\theta_{13} = 0$ causes the very long wavelength modes to be suppressed so that IceCube measures the average neutrino flux in half a year. The vacuum-oscillation average is obtained by dropping the off-diagonal terms of $\mathbf{V}\boldsymbol{\rho}$, *i.e.*, the neutrino density matrix in the mass basis. We ignore the attenuation of neutrinos as they pass through the Earth. Due to the low density of earth matter, attenuation becomes significant only above 10^5 GeV and is negligible for the atmospheric background and sub-TeV DM neutrino sources. Fig. 1 shows propagation effects on the neutrino spectra for Point A.

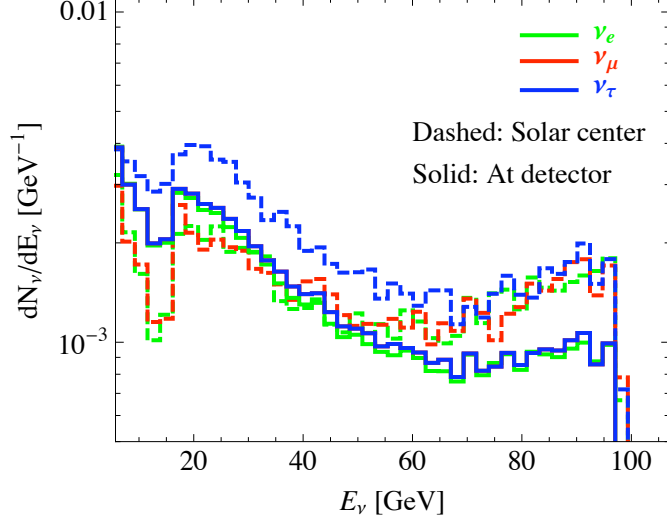


FIG. 1. Neutrino spectra for Point A at the center of the Sun (dashed) and at the detector (solid). The dominantly transverse WW channel leads to a hard spectrum. The attenuation is mainly due to CC scattering in the solar medium. NC scattering and τ -regeneration feed neutrinos back to lower energy. The spectra at the detector are time-averaged by removing vacuum oscillatory components. The ν_μ and ν_τ spectra at the detector are almost identical.

IV. DETECTOR SIMULATION

The IceCube detector is a km^3 sensor array that tracks muons. By selecting events that come from below the horizon, the only source of muons are the atmospheric and cosmic neutrinos that penetrate the bulk of the Earth and CC scatter with nuclei inside or in the vicinity of the detector. The detected muons are grouped into two categories: ‘contained’ muons with tracks starting within the instrumented volume, and ‘up-going’ muons that are created under the detector and range into the detector [19]. DeepCore is an extension with six additional strings inside the IceCube array. DC has a muon detection threshold as low as 10 GeV and vetoes all the muons detected by the surrounding IceCube strings, thus eliminating most of the huge downward muon background and allowing 4π detection of contained muons events. Recently Ref. [20] pointed out that cascade events may be detectable and may increase the event count at IceCube significantly. However, the angular resolution of cascade events is much poorer than track-like muon events, leading to a significantly larger acceptance cone size for atmospheric neutrinos. We found that the atmospheric cascade

event rate completely overwhelms the solar DM signal by a factor of $\sim 10^2$ even with an optimistic angular cone size of 30° . Consequently, we limit our study to track-like events.

The muon threshold energy has a significant effect on the background rates. Although IC and DC can detect muons with energy as low as 50 and 10 GeV respectively, the angular reconstruction for the muon track requires triggering of least three optical modules which raises the energy threshold. In most of what follows, we assume the threshold energy to be 100 GeV and 35 GeV for IC and DC, respectively, and the angular resolution to be 1° half apex angle.

The contained muons are detected at their initial (maximum) energy and the rate is given by

$$\frac{d\phi_\mu}{dE_\mu d\Omega} = V(E_\mu) \eta(\theta_z) \int_{E_\mu}^{E_\nu^{max}} dE_\nu \sum_{i=\nu_\mu, \bar{\nu}_\mu} n_{n/p} \frac{d\sigma_i^{n/p}(E_\nu, E_\mu)}{dE_\mu} \frac{d\phi_\nu^i}{dE_\nu}, \quad (8)$$

where $\frac{d\sigma^{n/p}}{dE_\mu}$ is the differential cross section of creating a muon of energy E_μ from CC scattering off a neutron/proton. $n_{n/p}$ is the numerical density of neutrons/protons in the medium and $\eta(\theta_z)$ is the detection efficiency at zenith angle θ_z . Note that at the South Pole the Sun stays within the range of $0 \sim 23^\circ$ from the horizon. We optimistically assume that the efficiency has a weak angular dependence and set $\eta = 1$. This gives the maximum muon count which can be further adjusted with realistic detector information. $\frac{d\phi_\nu}{dE_\nu}$ is the incoming neutrino flux at the detector. V is the detector volume which we take to be an energy-independent 1 km^3 for IC. For DC we parametrize the effective volume at SMT3-trigger level (DC veto) [21] as

$$V_{\text{DC}} = \begin{cases} 0.32 + 7.54x + 8.91x^2, & 0 < x \leq 1.09 \\ 11.9 + 7.77x - 1.06x^2, & 1.09 < x \leq 3.0 \\ 26.1, & x > 3.0 \end{cases} \quad (9)$$

where $x \equiv \log_{10}(E_\mu/\text{GeV})$ and V_{DC} is in megatons of water. The effective volume in ice is $V_{\text{DC}}^{\text{ice}} = V_{\text{DC}} \cdot \rho_{\text{water}}/\rho_{\text{ice}}$.

The up-going muons lose energy before reaching the detector modules. Muons with energy below a TeV lose energy mainly via ionization. Above a TeV, radiative losses becomes significant. Following Ref [22], the up-going muon rate is given by,

$$\frac{d\phi_\mu}{dE_\mu d\Omega} = A_\mu(E_\mu, \theta_z) \int_0^\infty dz \int_{E_\mu}^{E_\nu} dE_\mu^0 P(E_\mu^0, E_\mu; z)$$

$$\int_{E_\mu}^{E_\nu^{max}} dE_\nu \sum_{i=\nu_\mu, \bar{\nu}_\mu} n_{n/p} \frac{d\sigma_i^{n/p}(E_\nu, E_\mu^0)}{dE_\mu^0} \frac{d\phi_\nu^i}{dE_\nu}, \quad (10)$$

where E_μ^0 and E_μ denote the muon energy before and after propagating a distance z outside the detector. $P(E_\mu^0, E_\mu; z)$ is the survival probability of the muon after propagation which we simulate using the Muon Monte Carlo package [23]; for details see Appendix E. $A_\mu(E_\mu, \theta_z)$ is the effective muon detection area [22] parametrized by

$$A_\mu = 1\text{km}^2 \cdot A_0(E_\mu) (0.92 - 0.45 \cos \theta_z) \quad (11)$$

$$A_0 = \begin{cases} 0 & , \quad x < 1.6 \\ 0.784(x - 1.6) & , \quad 1.6 \leq x < 2.8 \\ 0.9 + 0.54(x - 2.8) & , \quad x \geq 2.8 \end{cases}$$

where $x \equiv \log_{10}(E_\mu/\text{GeV})$.

Observation of up-going events at IC starts with the September equinox ($t = 0$) and ends with the March equinox ($t = 0.5$). During this interval, the zenith angle of the Sun follows

$$\theta_z(t) = 90^\circ + 23.43^\circ \sin(2\pi t) \quad (0 \leq t \leq 0.5). \quad (12)$$

For IC, the muon rates are obtained by integrating Eq. 8 and Eq. 10 over the real-time zenith angle of the Sun; DC operates year-round so that observation time doubles. While the solar core is a point-like source, the major background for the DM signal comes from atmospheric neutrinos, which depends on the angular resolution of the detector. The directional atmospheric neutrino flux is measured by Super-K [24] and is symmetric about the horizon ($\theta_z = 90^\circ$). The left panel of Fig. 2 assumes a cone of 1° (half the apex angle) and shows the muon rate from atmospheric neutrinos at IceCube and DeepCore as a function of zenith angle. From the right panel it should be noted that the background rate increases quadratically with the opening angle of the acceptance cone. For a more detailed description of up-going and contained atmospheric background events, see Appendix C of Ref. [25].

V. DARK MATTER SIGNALS

The number of energetic neutrinos above detector threshold determine the prospects for detecting new physics at IceCube/DeepCore. For a solar WIMP signal there are three major

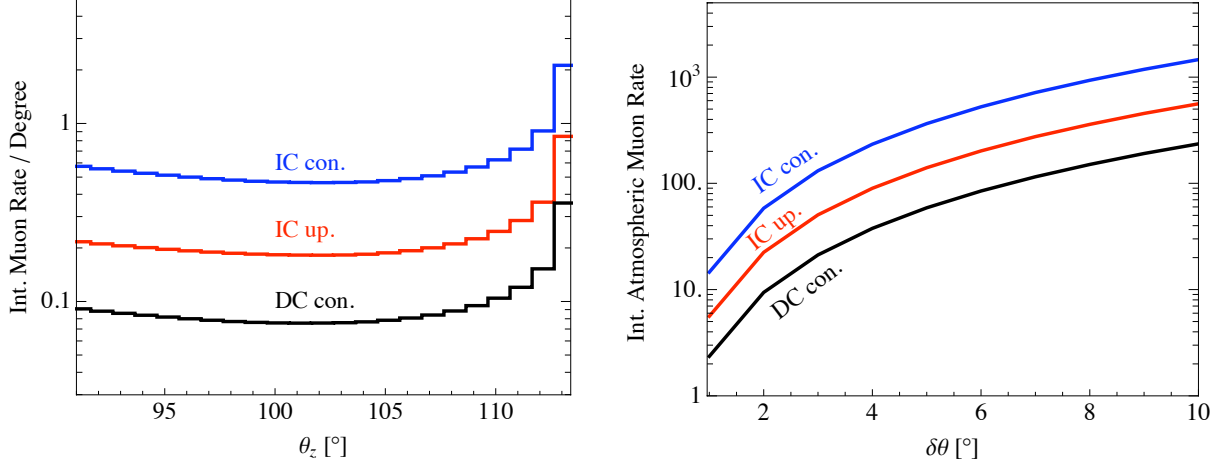


FIG. 2. Left panel: Integrated atmospheric background rate as the Sun sweeps through each degree in zenith angle in half-a-year at IceCube and a full-year at DeepCore assuming a 1° acceptance cone. Right panel: The acceptance cone-size $\delta\theta$ (half the apex angle) dependence of the yearly atmospheric background rates.

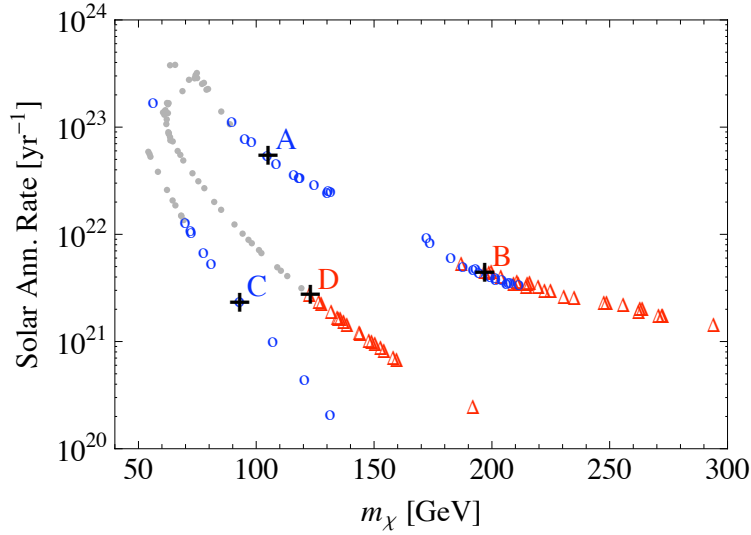


FIG. 3. Annihilation rate for mSUGRA points that are consistent with the measured relic density at the 95% C. L. Plotted points are from two scans in the $(m_0, m_{1/2})$ plane with $\tan\beta=10$ and 50. The light gray dots represent parameter points excluded by XENON100/Super-K/IC data. Points A–D of Table I are marked among the nonexcluded points with $\tan\beta=10$ (blue circles) and $\tan\beta=50$ (red triangles).

Source	IC up.	IC con.	IC up.	IC con.	DC
E_{thr}^{μ} (GeV)	100	100	70	70	35
Atm. bkg.	5.6	14	6.1	21	2.3
A	1.8×10^{-4}	0.042	8.2	9.7×10^2	196
B	2.4	66	5.4	1.7×10^2	21
C	0	0	0.016	2.9	2.2
D	0.011	1.3	0.18	14	3.2
E	3×10^{-5}	4×10^{-3}	6×10^{-4}	0.05	0.011
F	0	0	0	0	4.3
G	0	0	0	0	$\sim 10^{-6}$

TABLE II. Atmospheric background rate and signal rates for the points of Table I. The observation time for IC and DC are $\frac{1}{2}$ and 1 year, respectively. The acceptance cone has a 1° opening angle (half the apex angle) for both background and signal. E_{thr}^{μ} denotes the muon energy threshold.

factors: (i) annihilation rate; (ii) muon energy threshold vs. WIMP mass; (iii) annihilation channels that produce energetic neutrinos.

The relic density provides a stringent constraint that relates the first two factors. Fig. 3 illustrates the dependence of the yearly annihilation rate on the neutralino mass in different regions of mSUGRA parameter space. The inverse dependence of the annihilation rate on WIMP mass is evident with a minimum mass set by the energy threshold of the detector. Viable mSUGRA points must also be consistent with the XENON100 [26] constraint on σ_{SI} , which is the most stringent among nuclear recoil experiments [27], as well as the Super-K [28] and IC [29] constraints on σ_{SD} . The lower energy threshold of DeepCore greatly enhances the signal with respect to the background and can be crucial for WIMPs with mass $\sim 10^2$ GeV. The Focus Point region allows a large σ_{SD} coupling and is the most popular discovery scenario for mSUGRA. The $b\bar{b}$ channel generally produces less and softer neutrinos compared to the WW and ZZ channels. The $\tau^+\tau^-$ channel provides energetic neutrinos but often has a low branching fraction. The neutrino signal from a massive WIMP becomes hard to detect as the $b\bar{b}$ channel dominates (Point D).

In Table II, we list the signal rate for the points in Table I, and the atmospheric back-

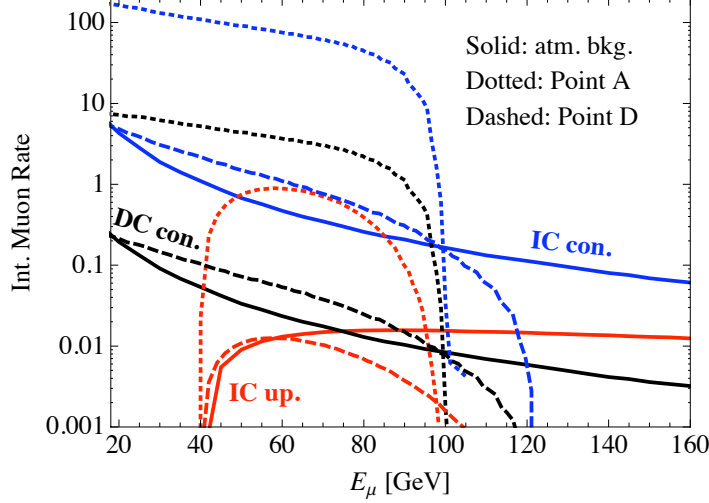


FIG. 4. Time-integrated muon energy spectra for the atmospheric background and WIMP signals.

ground rates; for IC we have entertained two possible detector thresholds for comparison. The differential energy spectra for Points A and D are shown in Fig. 4. With sufficient statistics as for Point A, it is even possible to construct the shape of the energy spectrum.

VI. SUMMARY

We presented a calculation of neutrino source spectra from solar dark matter annihilation, accounting for spin-correlations, and a simulation of the propagation and detection of these neutrinos at the IceCube/DeepCore detector. We considered the mSUGRA model to illustrate spin-correlations, but similar techniques can be applied to other WIMP models.

With an angular resolution of 1° half apex angle and muon energy threshold of 100 GeV and 35 GeV for IceCube and DeepCore respectively, the yearly atmospheric background rate is 5.6 for IC upgoing events, 14 for IC contained events and 2.3 for DC contained events. Generically, a neutralino annihilation rate of 10^{21} yr^{-1} is necessary to compete with the atmospheric background. With its lower energy threshold DC plays an important role in detecting neutrinos from relatively light ($\sim 10^2 \text{ GeV}$) dark matter candidates, which have less suppressed annihilation rates. For DM masses that are not much above the detector threshold, accounting for the helicity distribution of the final state particles can be critical for the detectability of the signal. For example, W pairs produced from neutralino annihilation are transversely polarized and give a much harder neutrino spectrum than if both helicities

contribute equally.

The neutrino-copious W^+W^- , $\tau^+\tau^-$ and $t\bar{t}$ channels are the main contributors to the neutrino signal. Since neutralinos are Majorana fermions, spin correlation requires W^+W^- to be transversely polarized which yields a hard neutrino spectrum and enhances the muon rate above IC/DC thresholds. The Focus Point region is the primary mSUGRA discovery region for IC/DC because of the high annihilation rate. In general, the neutrino signal rate can be compromised if the annihilation occurs primarily into channels that do not produce a significant neutrino flux or a hard spectrum.

ACKNOWLEDGMENTS

We thank Dmitry Chirkin, Tyce DeYoung, Arif Erkoca, Darren Grant, Francis Halzen, Jason Koskinen, Ina Sarcevic and Gabe Shaughnessy for useful discussions, and especially Enrico Maria Sessolo for many discussions and inputs. This work was supported by the DOE under Grant Nos. DE-FG02-04ER41308, DEFG02-95ER40896 and DE-FG02-96ER40969, by the NSF under Grant No. PHY-0544278, and by the Wisconsin Alumni Research Foundation.

Appendix A: Source neutrino spectrum

The primary channels that contribute neutrinos are given in Table III. Pre-shower spectra are generated with MadGraph/MadEvent (MG/ME) [30] or Calcchep [31] that keep the spin-correlation of the final state particles. We modified the MG/ME-Pythia [32, 33] interface to develop the shower and take into account the solar absorption of b, c hadrons. Secondary neutrinos come from subsequent decays of taus and b, c hadrons in the shower. In the case of τ decay, helicity information is facilitated by the Tauola [34] package, as part of the MG/ME-Pythia interface.

In the W^+W^- and $t\bar{t}$ channels, the undecayed W and t are made stable in the shower and their contribution is added as the charge conjugate of the neutrino spectra. Similarly, in the ZZ channel one Z boson is tagged stable in the shower and the neutrino spectrum is doubled. The $\tau^+\tau^-$ channel needs special treatment as a limitation of the LHE format [35]

Channel	Final state
W^+W^-	$W^{+*}\bar{\nu}_\tau\tau^-, W^{+*}s\bar{c}, W^{+*}d\bar{c}$
$t\bar{t}$	$t^*\bar{b}\bar{\nu}_\tau\tau^-, t^*\bar{b}s\bar{c}, t^*\bar{b}d\bar{c}$
ZZ	$Z^*\tau^+\tau^-, Z^*\nu_l^+\nu_l^-, Z^*b\bar{b}, Z^*c\bar{c}$
Zh	$h^*\tau^+\tau^-, h^*\nu_l^+\nu_l^-, h^*b\bar{b}, h^*c\bar{c},$ $Z^*\tau^+\tau^-, Z^*b\bar{b}, Z^*c\bar{c}$
$\tau^+\tau^-$	$\tau^+\tau^-$
$b\bar{b}$	$b\bar{b}$
$c\bar{c}$	$c\bar{c}$

TABLE III. Neutralino annihilation channels that contribute neutrinos. Particles marled with a * are made stable in the shower. The spin correlation in the $\tau^+\tau^-$ channel is treated separately with helicity-dependent decays.

makes it difficult to pass the $s/t/u$ channel particle information to Pythia, and Tauola cannot reconstruct the helicity of the pair-produced τ leptons. We circumvented this problem by treating τ decay analytically for the $\tau^+\tau^-$ channel, as discussed in Appendix B.

MadGraph has difficulty in producing transverse- W spectra for a few mSUGRA points in the static limit and we switched to Calchep for the W^+W^- channel. A drawback is that Calchep sums over final spins, so helicity information of the τ leptons is lost. Thus, most of the secondary (soft) ν_τ component in the W^+W^- channel is obtained from unpolarized τ decays. In the $t\bar{t}$ channel, final state radiation is turned off in Pythia to avoid a problem of flavor sum of parton clusters, after t is tagged stable. The resultant b quark energy may be high by a few percent. However, the effect is irrelevant since secondary neutrinos are dominantly produced from τ decay.

Appendix B: τ decay

While subdominant when the W^+W^- , ZZ and $t\bar{t}$ channels are kinematically allowed, the $\tau^+\tau^-$ channel is a major source of neutrinos for lighter DM as the other dominant channel, $b\bar{b}$, produces less neutrinos per annihilation. The relevant decay channels are $\tau \rightarrow \nu_\tau l \bar{\nu}_l$ and $\nu_\tau +$ hadrons as listed in Table IV. The neutrino energy spectrum in the rest frame of the τ

can be expanded as

$$\frac{1}{N_0} \frac{dN}{dx d\cos\theta} = f_0(x) + f_1(x) \cos\theta, \quad (\text{B1})$$

where $x = 2E_\nu/m_\tau$ is the energy fraction, and f_0, f_1 are projections of the distribution on the first two spherical harmonics. After boosting into the lab frame the first two harmonic coefficients are

$$\begin{aligned} g_0(y) &= \int_y^1 dx f_0(x)/x, \\ g_1(y) &= \int_y^1 dx (2y - x) f_1(x)/x^2, \end{aligned} \quad (\text{B2})$$

where $y = E_\nu/E_\tau$. The lab frame neutrino spectrum is

$$\frac{1}{N_0} \frac{dN}{dy} = g_0(y) + P g_1(y), \quad (\text{B3})$$

where $P = \pm 1$ for a left/right-handed τ . For a two-body decay $f_{0,1} = \delta(1 - x - m_X^2/m_\tau^2)$, while for the $\tau \rightarrow \nu_\tau l \bar{\nu}_l$ channel, these functions are [36]

$$f_0 = \begin{cases} 2x^2(3 - 2x) & \text{for } \nu_\tau \\ 12x^2(1 - x) & \text{for } \bar{\nu}_l \end{cases}, \quad f_1 = \begin{cases} -2x^2(2x - 1) & \text{for } \nu_\tau \\ 12x^2(1 - x) & \text{for } \bar{\nu}_l \end{cases}, \quad (\text{B4})$$

and the lab-frame spectra are listed in Table IV. For the short-lived mesons ρ and a_1 we smear the Dirac- δ to account for their widths. The rest-frame distributions are modified with a Breit-Wigner approximation,

$$f_{0,1} = \delta(1 - x - r_{mes}) \rightarrow f_{0,1}^* = C \frac{1}{(1 - x - r_{mes})^2 + m_{mes}^2 \Gamma_{mes}^2 m_\tau^{-4}}, \quad (\text{B5})$$

where $r_{mes} \equiv m_{\rho,a1}^2/m_\tau^2$, Γ_{mes} is the meson decay width and C is a normalization factor. The neutrino spectra resulting from left and right-handed τ decays are shown in Fig. 5.

Appendix C: Hadron absorption

Hadrons that contain c, b quarks contribute to the neutrino flux through their weak decay modes. However, the dense environment at the center of the Sun shortens the mean free path of these hadrons and absorption effects become significant when the mean free path

Decay mode (ν_τ)	BF	$g_0(y)$	$g_1(y)$
$\nu_\tau \ell \bar{\nu}_\ell$	0.18	$\frac{5}{3} - 3y^2 + \frac{4}{3}y^3$	$\frac{1}{3} + \frac{8}{3}y^3 - 3y^2$
$\nu_\tau \pi$	0.12	$\frac{1}{1-r_\pi} \theta(1-r_\pi-y)$	$-\frac{2y-1+r_\pi}{(1-r_\pi)^2} \theta(1-r_\pi-y)$
$\nu_\tau a_1$	0.13	$\int_y^1 f_0^*(x) x^{-1} dx$	$\int_y^1 (y-2x) f_1^*(x) x^{-2} dx$
$\nu_\tau \rho$	0.26	$\int_y^1 f_0^*(x) x^{-1} dx$	$\int_y^1 (y-2x) f_1^*(x) x^{-2} dx$
$\nu_\tau X$	0.13	$\int_y^1 f_X(x) x^{-1} dx$	0
Decay mode ($\bar{\nu}_l$)	BF	$g_0(y)$	$g_1(y)$
$\nu_\tau \ell \bar{\nu}_\ell$	0.18	$2 - 6y^2 + 4y^3$	$-2 + 12y - 18y^2 + 8y^3$

TABLE IV. τ decay modes, their branching fractions and fragmentation functions g_0 and g_1 . The smeared distributions f^* are as in Eq. B5. We approximated $f_X(y)$ for the inclusive $\tau \rightarrow \nu_\tau X$ channel with a generic phase-space decay into 4 pions and ν_τ .

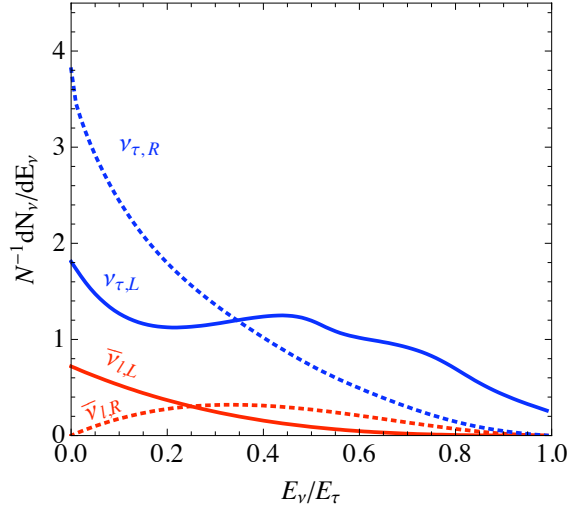


FIG. 5. $\nu_\tau, \bar{\nu}_l$ distribution from the decay of left(L)/right(R) handed taus.

is comparable to the decay length. We take the nucleon scattering cross sections of c, b hadrons [15] to be

$$\sigma(E) = \begin{cases} 1.4 \times 10^{-30} \text{ m}^2 & \text{for mesons} \\ 2.4 \times 10^{-30} \text{ m}^2 & \text{for baryons} \end{cases} \quad (\text{C1})$$

and the mean free path is

$$\lambda_s(E) = \frac{1}{n_\odot \sigma(E)}, \quad (\text{C2})$$

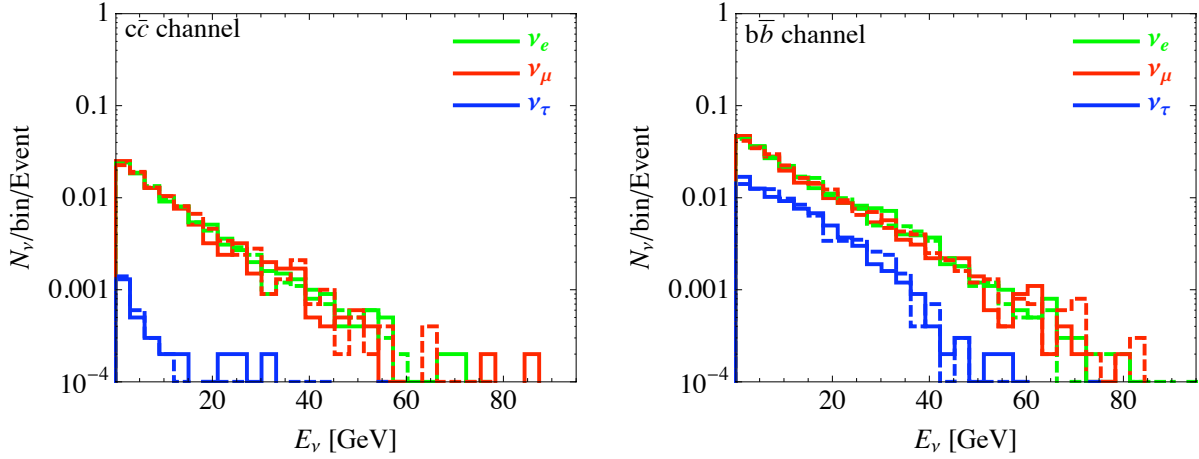


FIG. 6. Neutrino (solid) and antineutrino (dashed) spectra from the $c\bar{c}$ (left panel) and $b\bar{b}$ (right panel) channels for a 150 GeV WIMP.

where n_\odot is nucleon number density at the center of the Sun. The decay length is

$$\lambda_d(E) = c\tau\gamma(E), \quad (\text{C3})$$

where γ is the Lorentz boost factor, c is light speed and τ is rest-frame life time.

We assume that each scatter with a nucleus leaves the hadron with an average fraction $\epsilon = 0.7$ for b hadrons, and $\epsilon = 0.65 \frac{m_c}{m_{had}}$ for c hadrons [37] of the hadron's initial kinetic energy E_0 . After the n^{th} scattering, the ratio of the scattering probability to the decay probability is

$$\frac{P_{scattering}}{P_{decay}} = \frac{\lambda_d(E_n)}{\lambda_s(E_n)}, \quad (\text{C4})$$

where $E_n \sim E_0\epsilon^n$. We modified the Pythia package to simulate the decay and energy loss of c, b hadrons. The probability of scattering and decay are calculated iteratively for each hadron on an event by event basis. When a hadron is considered decayed, it is handed back to Pythia which develops the decay and showering. Since not all scatterings are elastic, we allowed the hadrons to scatter only once before decaying or being stopped/destroyed. The resultant neutrino spectra for a 150 GeV WIMP are shown in Fig. 6.

Appendix D: Neutrino scattering in propagation

The neutrino flux becomes attenuated by scattering off solar nuclei as it traverses the Sun. NC scattering decreases the neutrino energy while CC scattering converts the neutrino into the corresponding lepton whose decay introduces a secondary influx of less energetic neutrinos. The latter is often called “regeneration”. While electrons and muons are quickly absorbed by the dense solar medium, τ leptons decay promptly and contribute to the soft component of the neutrino flux.

The flux attenuation caused by NC scattering is flavor blind,

$$\left. \frac{d\boldsymbol{\rho}(E_\nu)}{dr} \right|_{NC}^{att.} = - n_{p/n} \sigma_{p/n}^{NC}(E_\nu) \boldsymbol{\rho}(E_\nu), \quad (D1)$$

where $\boldsymbol{\rho}$ is the flavor density matrix and $n_{p/n}$ is the solar proton/neutron number density [38]. The injection of scattered neutrinos is given by

$$\left. \frac{d\boldsymbol{\rho}(E_\nu)}{dr} \right|_{NC} = n_{p/n} \int_{E_\nu}^{E_\nu^{max}} dE'_\nu \frac{d\sigma_{p/n}^{NC}(E'_\nu, E_\nu)}{dE_\nu} \boldsymbol{\rho}(E'_\nu), \quad (D2)$$

where the dummy E'_ν integrates over energy above E_ν .

The attenuation via CC scattering is given by [16],

$$\left. \frac{d\boldsymbol{\rho}(E_\nu)}{dr} \right|_{CC}^{att.} = - \frac{\{\boldsymbol{\Gamma}_{CC}, \boldsymbol{\rho}\}}{2}, \quad (D3)$$

where $\boldsymbol{\Gamma}_{CC} = \mathbf{diag} (n_{p/n} \sigma_{p/n}^{CC}(E_\nu))$,

and the secondary contribution from τ regeneration is

$$\begin{aligned} \left. \frac{d\boldsymbol{\rho}_{ij}(E_\nu)}{dr} \right|_{CC}^{reg.} = & n_{p/n} \int_{E_\nu}^{E_\nu^{max}} dE'_\nu \int_{E_\nu}^{E'_\nu} \frac{dE_\tau}{E_\nu} \left[\right. \\ & \Pi_\tau \frac{d\sigma_{p/n}^{CC, \nu_\tau}(E'_\nu, E_\tau)}{dE_\tau} g_{\nu_\tau}(E_\nu/E_\tau) \boldsymbol{\rho}_{\tau\tau}(E'_\nu) \\ & \left. + \Pi_{e,\mu} \frac{d\sigma_{p/n}^{CC, \nu_e, \nu_\mu}(E'_\nu, E_\tau)}{dE_\tau} g_{\nu_{e,\mu}}(E_\nu/E_\tau) \bar{\boldsymbol{\rho}}_{\tau\tau}(E'_\nu) \right], \end{aligned} \quad (D4)$$

where $\Pi_l = \delta_{il}\delta_{jl}$ is a 3×3 matrix with only the l^{th} diagonal element nonzero and $l = 1, 2, 3$ for e, μ, τ respectively. Π_l picks out the diagonal terms from $\boldsymbol{\rho}$. $\bar{\boldsymbol{\rho}}$ denotes the density matrix for antineutrinos. Note that since neutrinos have definite helicity, the τ leptons from CC

scattering are polarized; τ^- is left-handed while τ^+ is right-handed. See Appendix B for the helicity fragmentation functions $g_{\nu_l}(y)$ for τ decay. The neutrino-nucleon scattering cross sections are evaluated with the numerical package Nusigma [39].

Appendix E: Muon propagation in ice

The muon energy spectrum $\phi_\mu(E_\mu, z)$ softens after propagation in ice, as generically described by

$$v_\mu \partial_z \phi_\mu(E_\mu, z) = - \int_0^{E_\mu} dE'_\mu \phi_\mu(E'_\mu, z) n(z) \frac{d\sigma(E_\mu, E'_\mu)}{dE'_\mu} + \int_{E_\mu}^{E_{max}} dE''_\mu \phi_\mu(E''_\mu, z) n(z) \frac{d\sigma(E''_\mu, E_\mu)}{dE''_\mu} + \partial_{E_\mu}(\alpha(E_\mu) \phi_\mu(E_\mu, z)), \quad (\text{E1})$$

where $v_\mu \approx c$ is the muon speed, σ is the muon scattering cross section, $n(z)$ is the target density, and α describes ionization energy losses. E_μ is the muon's energy at a propagated distance z and dummy variables E'_μ, E''_μ denote the energy below/above E_μ . In terms of the survival probability $P(E_\mu^0, E_\mu; z)$, the final energy spectrum can be written as

$$\phi_\mu(E_\mu, z) = \int P(E'_\mu, E_\mu; z - z_0) \phi_\mu(E'_\mu, z_0) dE'_\mu, \quad (\text{E2})$$

where E_μ^0 is the initial muon energy. For $z \neq 0$, $P(E_\mu^0, E_\mu; z)$ can be below unity upon integration over E_μ due to muons being stopped before reaching z ; $P(E_\mu^0, E_\mu; z)$ can be obtained from Monte Carlo simulations.

The spatial integral in Eq. 10 can be done separately to yield the so-called “effective muon range” [22],

$$R(E_\mu^0, E_\mu) = \int_0^\infty P(E_\mu^0, E_\mu; z) dz. \quad (\text{E3})$$

$R(E_\mu^0, E_\mu)$ represents the average incremental distance a muon travels per unit energy loss (in GeV) at E_μ .

The average neutrino effective area is [22],

$$A_\nu^{eff}(E_\nu, \theta_z) = \frac{1}{2} \sum_{i=\nu_\mu, \bar{\nu}_\mu} \int dE_\mu dE_\mu^0 n_{n/p} \frac{d\sigma_i^{n/p}(E_\nu, E_\mu^0)}{dE_\mu^0} R(E_\mu^0, E_\mu) A_\mu(E_\mu, \theta_z), \quad (\text{E4})$$

where $A_\mu(E_\mu, \theta_z)$ is the muon effective area given by Eq. 11. The attenuation of sub-TeV neutrinos inside the Earth can be ignored.

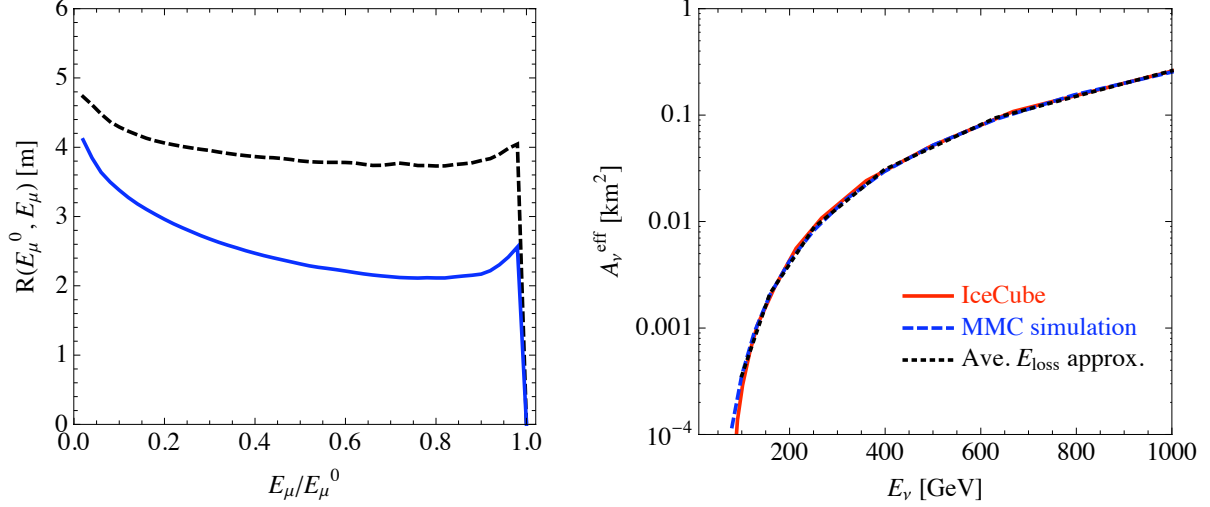


FIG. 7. Left panel: Differential effective range $R(E_\mu^0, E_\mu)$ in ice for 100 GeV (dashed) and 1 TeV (solid) muons. Right panel: Comparison of A_ν^{eff} from the IceCube detector simulation [22], our simulation with MMC, and the approximate method using a parameterization of average neutrino energy losses. The plotted A_ν^{eff} is an angular average over $\theta_z > 90^\circ$. With $\alpha = 2.5 \times 10^{-3} \text{ GeV cm}^2/\text{g}$, $\beta = 4 \times 10^{-6} \text{ cm}^2/\text{g}$, the average E_ν loss method agrees well with sophisticated simulations.

We used Muon Monte Carlo (MMC) to simulate the muon survival probability $P(E_\mu^0, E_\mu; z)$. The interpolated effective range for 100 GeV and 1 TeV muons are shown in Fig. 7. As a test we calculated A_ν^{eff} and compared to the full detector simulation, and found excellent agreement as is evident from Fig. 7.

Alternatively, a frequently used approximation for muon propagation parameterizes the average muon energy loss,

$$\frac{dE_\mu}{dz} = -\rho(\alpha + \beta E_\mu), \quad (\text{E5})$$

where ρ is the medium density and α, β account for ionization and radiative effects. This procedure ignores the smearing of the muon energy distribution during propagation. For ice, we found $\alpha = 2.5 \times 10^{-3} \text{ GeV cm}^2/\text{g}$, $\beta = 4 \times 10^{-6} \text{ cm}^2/\text{g}$ agrees well with the MMC results, as shown in Fig. 7. There is a mild degeneracy in the parameters α and β , so that $\alpha = 3 \times 10^{-3} \text{ GeV cm}^2/\text{g}$, $\beta = 3 \times 10^{-6} \text{ cm}^2/\text{g}$ [25], works just as well.

-
- [1] G. R. Farrar and P. Fayet, Phys. Lett. B **76**, 575 (1978). S. Dimopoulos and H. Georgi, Nucl. Phys. B **193**, 150 (1981). G. R. Farrar and S. Weinberg, Phys. Rev. D **27**, 2732 (1983). N. Sakai and T. Yanagida, Nucl. Phys. B **197**, 533 (1982).
 - [2] N. Jarosik *et al.*, arXiv:1001.4744 [astro-ph.CO].
 - [3] A. H. Chamseddine, R. L. Arnowitt and P. Nath, Phys. Rev. Lett. **49**, 970 (1982). R. Barbieri, S. Ferrara and C. A. Savoy, Phys. Lett. B **119**, 343 (1982). L. J. Hall, J. D. Lykken and S. Weinberg, Phys. Rev. D **27**, 2359 (1983).
 - [4] Y. B. Zeldovich, A. A. Klypin, M. Y. Khlopov and V. M. Chechetkin, Sov. J. Nucl. Phys. **31** (1980) 664 [Yad. Fiz. **31** (1980) 1286]. J. Silk, K. A. Olive and M. Srednicki, Phys. Rev. Lett. **55**, 257 (1985). L. M. Krauss, K. Freese, W. Press and D. Spergel, Astrophys. J. **299**, 1001 (1985). T. K. Gaisser, G. Steigman and S. Tilav, Phys. Rev. D **34**, 2206 (1986). L. M. Krauss, M. Srednicki and F. Wilczek, Phys. Rev. D **33**, 2079 (1986).
 - [5] W. H. Press and D. N. Spergel, Astrophys. J. **296**, 679 (1985).
 - [6] A. Gould, Astrophys. J. **328**, 919 (1988).
 - [7] For a recent progress report on IceCube: K. Hultqvist, for the IceCube Collaboration, arXiv:1003.2300 [astro-ph.HE].
 - [8] C. Wiebusch, for the IceCube Collaboration, arXiv:0907.2263 [astro-ph.IM].
 - [9] V. Barger, D. Marfatia, A. Mustafayev and A. Soleimani, Phys. Rev. D **80**, 076004 (2009) [arXiv:0908.0941 [hep-ph]].
 - [10] H. Baer, A. Mustafayev, E. K. Park and X. Tata, JHEP **0805**, 058 (2008) [arXiv:0802.3384 [hep-ph]].
 - [11] G. Jungman, M. Kamionkowski and K. Griest, Phys. Rept. **267**, 195 (1996) [arXiv:hep-ph/9506380].
 - [12] M. Kamionkowski, Phys. Rev. D **44**, 3021 (1991).
 - [13] J. Ellis, K. A. Olive, C. Savage and V. C. Spanos, Phys. Rev. D **81**, 085004 (2010) [arXiv:0912.3137 [hep-ph]].
 - [14] K. Griest and D. Seckel, Nucl. Phys. B **283**, 681 (1987) [Erratum-ibid. B **296**, 1034 (1988)].
 - [15] J. Edsjo, arXiv:hep-ph/9704384. B. Povh and J. Hufner, Phys. Lett. B **245** (1990) 653.

- [16] A. Strumia and F. Vissani, arXiv:hep-ph/0606054.
- [17] L. Wolfenstein, Phys. Rev. D **17**, 2369 (1978). V. Barger, K. Whisnant, S. Pakvasa, and R. J. N. Phillips, Phys. Rev. D **22**, 2718 (1980). S. P. Mikheev and A. Y. Smirnov, Sov. J. Nucl. Phys. **42**, 913 (1985).
- [18] M. Maltoni, T. Schwetz, M. A. Tortola and J. W. F. Valle, New J. Phys. **6**, 122 (2004) [arXiv:hep-ph/0405172].
- [19] A. E. Erkoca, M. H. Reno, I. Sarcevic, Phys. Rev. **D80**, 043514 (2009). [arXiv:0906.4364 [hep-ph]].
- [20] M. D’Agostino, for the IceCube Collaboration, arXiv:0910.0215 [astro-ph.HE]; arXiv:0910.2555 [astro-ph.HE].
- [21] T. DeYoung and J. Koskinen, private communication.
- [22] M. C. Gonzalez-Garcia, F. Halzen and S. Mohapatra, Astropart. Phys. **31**, 437 (2009) [arXiv:0902.1176 [astro-ph.HE]].
- [23] D. Chirkin and W. Rhode, arXiv:hep-ph/0407075.
- [24] M. Honda, T. Kajita, K. Kasahara, S. Midorikawa and T. Sanuki, Phys. Rev. D **75**, 043006 (2007) [arXiv:astro-ph/0611418].
- [25] V. Barger, J. Kumar, D. Marfatia and E. M. Sessolo, Phys. Rev. D **81**, 115010 (2010) [arXiv:1004.4573 [hep-ph]].
- [26] E. Aprile *et al.* [XENON100 Collaboration], arXiv:1005.0380 [astro-ph.CO].
- [27] For a recent review of direct searches, see A. M. Szelc, Acta Phys. Polon. B **41**, 1417 (2010), and references therein.
- [28] S. Desai *et al.* [Super-Kamiokande Collaboration], Phys. Rev. D **70**, 083523 (2004) [Erratum-ibid. D **70**, 109901 (2004)] [arXiv:hep-ex/0404025].
- [29] R. Abbasi *et al.* [IceCube Collaboration], Phys. Rev. Lett. **102**, 201302 (2009) [arXiv:0902.2460 [astro-ph.CO]].
- [30] J. Alwall *et al.*, JHEP **0709**, 028 (2007) [arXiv:0706.2334 [hep-ph]].
- [31] A. Pukhov *et al.*, arXiv:hep-ph/9908288. A. Pukhov, arXiv:hep-ph/0412191.
- [32] T. Sjostrand, S. Mrenna and P. Z. Skands, JHEP **0605**, 026 (2006) [arXiv:hep-ph/0603175].
- [33] Parton showering, hadronization and detector simulation for MadGraph/MadEvent available from <http://madgraph.hep.uiuc.edu/index.html>

- [34] Z. Was, Nucl. Phys. Proc. Suppl. **189**, 43 (2009) [arXiv:0901.1865 [hep-ph]].
- [35] J. Alwall *et al.*, Comput. Phys. Commun. **176**, 300 (2007) [arXiv:hep-ph/0609017]. B. Allanach *et al.*, Comput. Phys. Commun. **180**, 8 (2009) [arXiv:0801.0045 [hep-ph]].
- [36] P. Lipari, Astropart. Phys. **1** (1993) 195.
- [37] S. Ritz and D. Seckel, Nucl. Phys. B **304**, 877 (1988).
- [38] J. N. Bahcall, S. Basu, M. Pinsonneault, and A. M. Serenelli, Astrophys. J. **618**, 1049 (2005), astro-ph/0407060.
- [39] M. Blennow, J. Edsjo and T. Ohlsson, JCAP **0801**, 021 (2008) [arXiv:0709.3898 [hep-ph]]; the *Nusigma* code is available from the WimpSim website <http://www.physto.se/~edsjo/wimpsim/code.html>